Journal of Cardiovascular Magnetic Resonance (2005) **7,** 501–516

ISSN: 1097-6647 print / 1532-429X online
DOI: 10.1081/JCMR-200053610

Taylor & Francis
Taylor & Francis Group

REVIEW

Assessment of myocardial function: a review of quantification methods and results using tagged MRI

CAROLINE PETITJEAN, PH.D.,[1] NICOLAS ROUGON, PH.D.,[1] and PHILIPPE CLUZEL, M.D., PH.D.[2,*]

[1]*ARTEMIS Project Unit, GET/INT, Evry, France*
[2]*Service de Radiologie Polyvalente Diagnostique et Interventionnelle, Groupe Hospitalier Pitié-Salpêtrière, Paris, France*

Tagged MRI provides a noninvasive way to assess the regional function of the heart. Clinical use of myocardial strain measurements from tagged MRI requires identifying new normative values. As for cardiac motion estimation, a variety of methods for quantifying myocardial deformations have been proposed in the image analysis and medical literature, based on heart geometry and continuum mechanics. This article comparatively reviews existing quantification techniques, and synthesizes their results to establish confidence intervals for the standard deformation parameters.

Key Words: Myocardial function; Myocardial strain measurement; Tagged magnetic resonance imaging

1. Introduction

Tagged MRI is the reference MR modality to assess the regional function of the heart (1, 2). Measuring myocardial deformations from tagged MR image sequences relies on 1) estimating a dense motion field, and 2) computing local and segmental deformation parameters over the myocardium. In this paper, the focus is set on the second step. The clinical use of myocardial strain information derived from tagged MRI requires identifying new normative values. Based on a synthesis of the numerous contributions published in this field, this article aims at establishing confidence intervals for the standard deformation parameters.

The literature on myocardial strain measurement can be divided into technical studies (TS) that emphasize motion estimation, and medical studies (MS) that focus on quantification of material properties. We have reviewed 20 medical articles and eight technical papers issued between 1991 and 2003. The studies dedicated to the left ventricle (LV) are listed in Table 1, whereas Table 2 presents the studies focusing on the right ventricle (RV). Synthesizing their results requires taking into account:

- External parameters, such as population (age, gender, heart rate, etc.), MR acquisition parameters (number of slices, slice incidence, temporal and spatial resolutions), and MR tagging parameters (tagging pattern, tag orientation, spacing, etc.). This is the subject of Section 2.
- The methods for motion estimation and deformation measurement that are reviewed in Section 3.

Quantitative results are presented and discussed in Section 4. In a final section, conclusions are drawn about common trends and disparities encountered when characterizing the behavior of the healthy human heart.

2. Materials

2.1. *Population*

Most of the studies aim at characterizing a pathology (e.g., hypertrophic cardiomyopathy, myocardial infarction, idiopathic dilated cardiomyopathy, aortic stenosis), and usually include a control group of healthy volunteers. Since this paper is targeted at characterizing the normal human heart, we have only accounted for this group. Whereas the results reported in TS often deal with a single person, MS use a number of subjects (mean ± SD: 18 ± 20 subjects, ranging from three to 87). Population age is a significant parameter that is provided by 18/20 MS vs. 2/8 TS. Some studies use an age-matched control group when comparing to a patient group. Gender and heart rates are also of interest.

2.2. *MR acquisition*

Among the many available MR tagging techniques, SPAMM (SPAtial Modulation of Magnetization) (2) is the most widely

Received 10 September 2003; accepted 11 November 2004.
*Address correspondence to Philippe Cluzel, M.D., Ph.D., Service de Radiologie Polyvalente Diagnostique et Interventionnelle, Groupe Hospitalier Pitié-Salpêtrière, 47-83 Boulevard, de l'Hôpital, 75651 Paris Cedex 13, France; Fax: +33-1-42-17-73-36; E-mail: philippe.cluzel@psl.ap-hop-paris.fr

Table 1. Medical (*above*) and technical (*below*) studies assessing LV contraction in tagged MR images

Reference	Estimation method	Population				Acquisition parameters							Regional differentiation				Param. type
		Nb	Age	M/F	Patho	FOV	ST	TS	SR	TpR	TR/TE/ϕ	Tag					
Clark et al. (46)	VIDA	10	23 to 34	5/5		240	5	7	0.88	60	RR/20/–	SPAMM			R	C	L	E
Rogers et al. (44)	–	19	56 ± 17	14/5		–	–	–	–	–	RR/30/–	3 lines				C	L	D
Kramer et al. (28)	VIDA	10	27	–	HCM	400	5	7	–	–	RR/20/–	SPAMM		T		C	L	E
Dong et al. (29)	Manual	6	46 ± 14	5/1	HCM	320	10	–	–	–	–	Radial				C	L	E
Young et al. (26)	SPAMMVU	12	19 to 37	6/6	HCM	240	5	7	–	–	–	SPAMM				C	L	D, S
Chai et al. (30)	Manual	9	20 to 35	5/6		200	8	–	5.8	–	–/20/–	SPAMM					L	E
MacGowan et al. (24)	(3, 4)	9	–	–	IDC	–	–	–	–	–	–	Radial			R			S
Stuber et al. (42)	Snakes	11	34 ± 9	–	AS	360	6	–	1.4	35	–/3.4/–	CSPAMM		T				D, V
Garot et al. (31)	HARP	10	37 ± 10	–	MI	360	8	7	–	–	6.5/2.3/15	SPAMM	d		R	C	L	E, S
Moore et al. (39)	FindTags	31	37 ± 11	16/15		360	–	6	–	32.5	6.5/2.1/12	SPAMM		T	R	C	L	D, S
Nagel et al. (43)	–	12	29 ± 6	8/4	AS	–	6/8	8	1.4	35	3200/54/–	CSPAMM		T			L	D
Bogaert et al. (5)	–	30	59 ± 7	20/11	MI	–	8	–	–	–	14/8/–	Radial			R			E
Bogaert et al. (23)	–	87	44 ± 15	56/31		–	–	–	–	–	–	Radial			R	C	L	E
Götte et al. (6)	SPAMMVU	13	53 ± 7	13/0	MI	220	6	7	–	40	RR/20/–	SPAMM				C		S
Ennis et al. (7)	FindTags	3	59 ± 5	–	HCM	–	–	–	–	–	–	CSPAMM		T		C		S
Dornier et al. (45)	HARP	20	29 ± 7	–	MI	–	8	7	–	–	7.6/6.2/15	Philips				C		S
Kuijer (36)	SPAMMVU	10	46 ± 11	10/0		250	6	7	–	30	10/3.8/15	SPAMM		T		C	L	S
Oxenham (37)	Snakes	31	22/69	–		–	7	–	1	35	–	SPAMM		T				D, S
Park et al. (18)	Def.model	–	–	–	HCM	–	–	–	–	–	–	SPAMM	d	T	R		L	D
Declerck et al. (14)	Parametric	1	–	1/0	MI	320	–	–	–	40	3.6/1.5/12	SPAMM		T		C	L	D, S
Osman et al. (11)	HARP	1	–	1/0		–	–	–	1.25	32.5	–	SPAMM	d	T				E
Clarysse et al. (15)	FindTags	1	–	1/0	MI	–	–	–	–	–	10/4/15	DANTE		T	R			S
Allouche et al. (40)	Tag model	15	–	14/1		–	8	–	1.17	35	–	CSPAMM		T	R		L	D

Population: Nb is the number of healthy volunteers. Age is given as mean ± SD years. Gender is given as men number/women number.
Pathologies: HCM = hypertrophic cardiomyopathy, MI = myocardial infarction, IDC = idiopathic dilated cardiomyopathy, AS = aortic stenosis.
Acquisition parameters: FOV = field of view (mm), ST = slice thickness (mm), TS = tag spacing (mm), SR = spatial resolution (mm), TpR = temporal resolution (ms), TR/TE/ϕ = repetition time (ms)/echo time (ms)/flip angle (degrees).
Regional differentiation: d = dense, R = radial, C = circumferential, L = longitudinal, T = temporal.
Parameter type: V = velocity, D = displacement, E = elongation, S = strain.

Table 2. Medical (*above*) and technical (*below*) studies assessing RV contraction in tagged MR images

Reference	Estimation method	Population				Acquisition parameters							Segmentation
		Nb	Age	M/F	Patho	FOV	ST	TS	SR	TpR	TR/TE/ϕ	Tag	
Naito et al. (32)	Manual	9	32 ± 4	9/0		350	10	12/25	–	–	RR/8/30	2 lines	3S
Young et al. (48)	SPAMMVU	1	–	–	RVH	400	6	7	–	–	8.3/2.5/–	SPAMM	
Fayad et al. (33)	SPAMMVU	10	28	5/5	cPH	220	6	7	–	–	8/2.6/15	SPAMM	A
Klein et al. (34)	Manual	16	25 ± 1	11/5		350	7	7/8	–	–	50/–/–	Grid	3S
Haber et al. (47)	SPAMMVU	2	–	–	RVH	260	6	8	–	–	7/2.6/	SPAMM	

Population: Nb is the number of healthy volunteers. Age is given as mean ± SD years. Gender is given as men number/women number.
Pathologies: RVH = right ventricular hypertrophy, cPH = chronic pulmonary hypertension.
Acquisition parameters: FOV = field of view (mm), ST = slice thickness (mm), TS = tag spacing (mm), SR = spatial resolution (mm), TpR = temporal resolution (ms), TR/TE/ = repetition time (ms)/echo time (ms)/flip angle (degrees).
Segmentation type: 3S = three segments, A = anatomical.

used. Alternative technologies include DANTE (Delays Alternating with Nutations for Tailored Excitations) (8) and CSPAMM (Continuous SPAMM) (9). The tagging pattern can be linear, rectangular or, more rarely, radial (3/20 MS vs. no TS). Tagged MR images are obtained in the short-axis view and/or the horizontal longaxis (also called four-chamber) view (Fig. 1). Regarding MR acquisition parameters, more information is available in MS than in TS. Surprisingly, though being one of the most significant parameters, tag spacing is reported in only 10/20 MS and 2/8 TS (cf. Tables 1–2).

3. Methods

3.1. *Motion estimation*

The motion estimation techniques proposed in TS (10) can be divided into 1) differential optical flow-based methods, which often require knowing acquisition parameters and fail to deal with large deformations due to their local nature; 2) phase-based optical flow methods such as HARP, which are sensitive to artifacts (11); and 3) tag segmentation methods, followed by sparse motion estimation along the tagging pattern and dense motion interpolation over the whole image domain (12–15).

MS usually make use of available motion estimation software packages, such as:

- FindTags (13) or SPAMMVU (16), which rely on segmentation-based methods.
- HARP (11), which implements a phase-based method.

MS also resort to manual supervision, including delineation of the epicardium and endocardium, and designation of tag intersections or tag-ventricle boundaries intersections. In this case, intra- and inter-observer variability can be assessed by performing blinded paired measurements (46).

3.2. *Deformation measurement*

The LV myocardium has a complex architecture: fibers in the midwall are circumferential, whereas subepicardial and subendocardial fibers are almost longitudinally directed (Fig. 2). This results in inhomogeneous and complex contraction patterns, correlated to fiber structure. LV deformations comprise radial thickening, circumferential shortening, torsion, and longitudinal shortening.

In the RV, fibers are mainly longitudinally oriented, so that the complex RV motion is, in general, oriented in a similar direction. Only a few studies have attempted to quantify RV motion, in large part due to its thin wall and complex geometry. Currently, noninvasive assessment of RV contractility remains extremely difficult with conventional techniques (17).

Measuring myocardial deformations requires defining a reference coordinate system. Deformation parameters then divide into zero-order parameters, which are derived directly from displacement data, and first-order parameters, such as strains and shears, which are extracted from the strain tensor.

3.1.1. *Reference coordinate system*

The Radial-Circumferential-Longitudinal (RCL) coordinate system (Fig. 3) is widely used due to its suitability for modeling LV geometry.[a] The Radial-Fiber-Cross-Fiber (RFCF) coordinate system (Fig. 3), based on fiber direction, requires a precise knowledge of their orientation angles. Diffusion MR imaging can determine fiber angles in vivo (19–22) but is not available for general clinical use. Fiber directions have then to be obtained from histological fiber angles in cadaver studies (23). Errors could result from population mismatching (24).

3.2.2. *Displacement*

The coordinates of a myocardial point during the cardiac cycle are related by displacement. Specifically, denoting by $\mathbf{x}$ and $\mathbf{x}'$ its position at times t and $t' > t$, respectively, one has:

$$\mathbf{x}' = \mathbf{x} + \mathbf{u}(\mathbf{x}) := \mathbf{f}(\mathbf{x}) \quad (1)$$

where $\mathbf{u}$ is the *displacement* and $\mathbf{f}$ is referred to as the *deformation*.

[a]In contrast, the rectangular Cartesian coordinate system is used only once in Ref. (18).

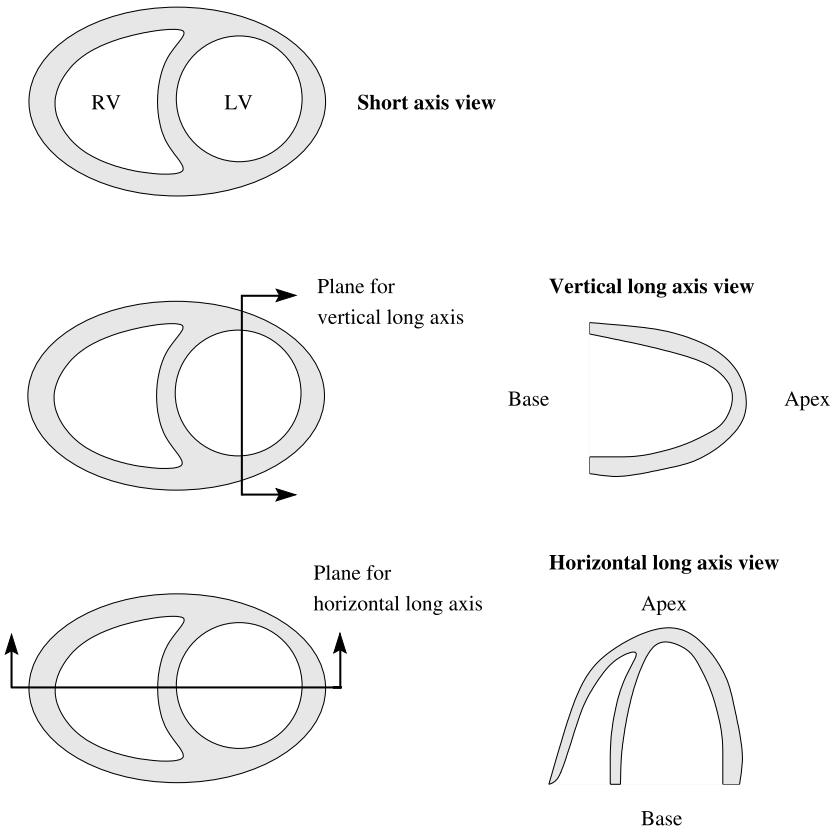

Figure 1. Cardiac imaging plane definition.

The motion distribution along specific directions is captured by *directional displacement*. More precisely, the displacement along a direction $\mathbf{d}$ ($\|\mathbf{d}\| = 1$) is defined as the component $\mathbf{u_d} := (\mathbf{d}^T\mathbf{u})\ \mathbf{d}$ of the displacement $\mathbf{u}$ along the vector $\mathbf{d}$, where $\mathbf{d}^T$ denotes the transposed vector of $\mathbf{d}$ (Fig. 4).

Relevant choices for $\mathbf{d}$ are related to myocardial anatomy and depend on the viewing axis. For short-axis views, displacements are assessed along the normal and tangential directions to myocardial boundaries (Fig. 5). For long-axis views, longitudinal displacements along the long axis of the heart and radial displacements perpendicular to this axis are computed (Fig. 6).

In short-axis views, one may also assess the LV local rotation angle or the torsion. The latter is defined as the rotation of the apex about the long axis relative to the base.

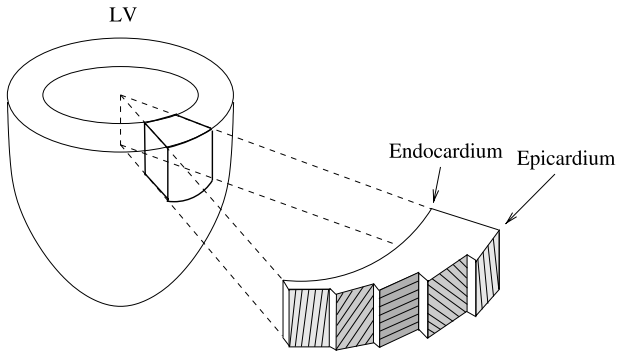

Figure 2. Fiber orientation in the LV.

3.3.3. *Strain and shear*

The relative variations of distance between myocardial points during the heart deformation are described by *strain* and *shear*. Several approaches for defining these parameters are reported in the literature, resulting in a variety of mathematical expressions with no straightforward connections:

- Considering spatial variations of the displacement magnitude of material points leads to definitions based on the *strain tensor*, denoted by $\mathbf{E}$ and such that:

$$\mathrm{E} := \frac{1}{2}(\nabla \mathrm{u} + \nabla \mathrm{u}^T + \nabla \mathrm{u}^T \nabla \mathrm{u}) \tag{2}$$

where ∇ is the gradient operator. Equation 1 yields equivalently:

$$\mathrm{E} := \frac{1}{2}(\mathrm{F}^T\mathrm{F} - \mathrm{Id}) \tag{3}$$

where $\mathbf{F} := \nabla\mathbf{f}$ is the deformation gradient tensor and $\mathbf{Id}$ the identity.

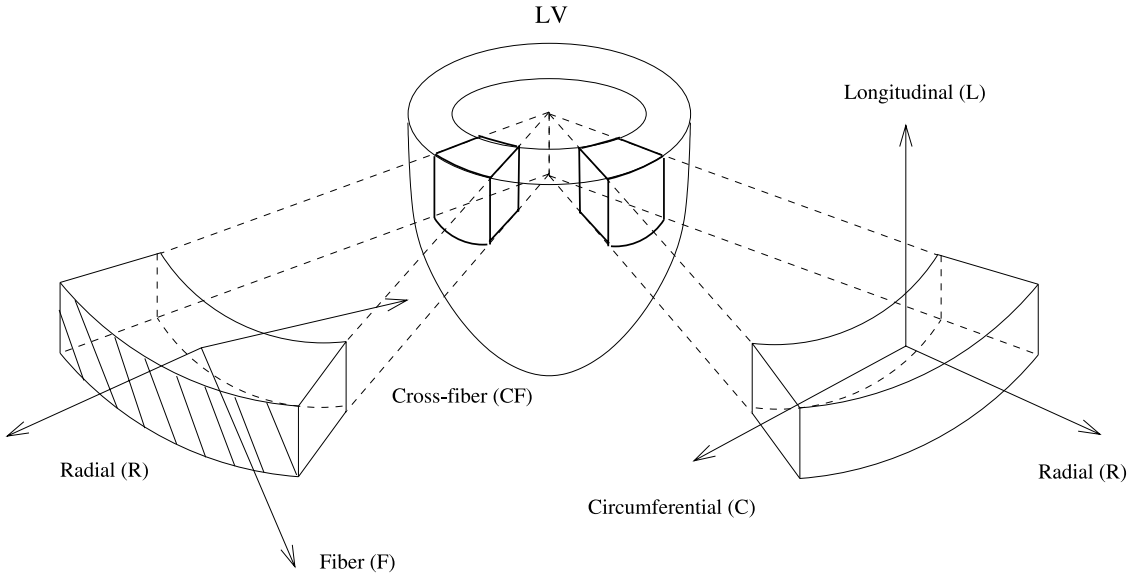

Figure 3. The two conventional LV coordinate systems. The RCL system includes radial (R), circumferential (C) and longitudinal (L) directions. The RFCF system includes radial (R), fiber (F) and cross-fiber (CF) directions.

- Alternatively, one can consider relative variations of the length of material segments.

In what follows, the various definitions for strain and shear are summarized, and shown to be equivalent in the case of small deformations.

3.3.3.1. *Strain*. The diagonal elements E_{ii} of the strain tensor $\mathbf{E} = (E_{ij})$ define *normal strains* (Fig. 7). They represent the magnitude of stretching ($E_{ii} > 0$) or shortening ($E_{ii} < 0$) along coordinate axes. More generally, a directional strain along some unit vector $\mathbf{v}$ is defined as:

$$Q_{\mathrm{v}} := \mathrm{v}^T \mathrm{E} \mathrm{v} \tag{4}$$

Strain reflects therefore both the direction and the spatial variations of displacement (Fig. 8).

For 3D displacement fields, three normal strains can be computed at each point. Measuring radial, circumferential, and longitudinal strains is achieved by computing either the strain tensor in the RCL coordinate system (14, 15, 25, 26), or the directional strain $Q_{\mathbf{v}}$ along a vector $\mathbf{v}$ pointing in the radial, circumferential and longitudinal direction, respectively (27).

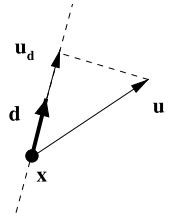

Figure 4. Directional displacement $\mathbf{u_d}$ along the unit vector $\mathbf{d}$, derived from displacement $\mathbf{u}$ at point $\mathbf{x}$.

An alternate approach, widely used in MS (23, 28–34), considers relative directional variations of the length of material segments. Analysis of deformations between end diastole (ED) and end systole (ES) then permits the definition of *elongation* along a unit vector $\mathbf{v}$, denoted by $\varepsilon_{\mathbf{v}}$, as:

$$\varepsilon_{\mathrm{v}} := \frac{\|\mathrm{dp}_{ES}\| - \|\mathrm{dp}_{ED}\|}{\|\mathrm{dp}_{ED}\|} \tag{5}$$

where $\mathbf{dp}_{ED}$ and $\mathbf{dp}_{ES}$ denote a material segment lying along the vector $\mathbf{v}$ (i.e., $\mathbf{dp} = \|\mathbf{dp}\|\mathbf{v}$) at ED and ES, respectively.[b,c]

Using squared distances in Eq. 4 yields another strain measure, denoted by $\varepsilon_{\mathbf{v}}^{(2)}$

$$\varepsilon_{\mathrm{v}}^{(2)} := \frac{\|\mathrm{dp}_{ES}\|^2 - \|\mathrm{dp}_{ED}\|^2}{\|\mathrm{dp}_{ED}\|^2} \tag{6}$$

As shown in Appendix A, the latter verifies:

$$\varepsilon_{\mathrm{v}}^{(2)} = 2Q_{\mathrm{v}} \tag{7}$$

Combining Eqs. 4–6 yields the connection identity (35–37):

$$\varepsilon_{\mathrm{v}} = \sqrt{1 + 2Q_{\mathrm{v}}} - 1 \tag{8}$$

[b]Elongation is also defined as $-\varepsilon_{\mathbf{v}}$, which ensures consistency with the definitions of ejection and shortening fractions. The sign convention for strain is then reversed: shortening and lengthening correspond to negative and positive values, respectively.

[c]Definition (4) is often multiplied by 100 to express elongation as a percentage. We adopt this convention in the remaining part of this paper.

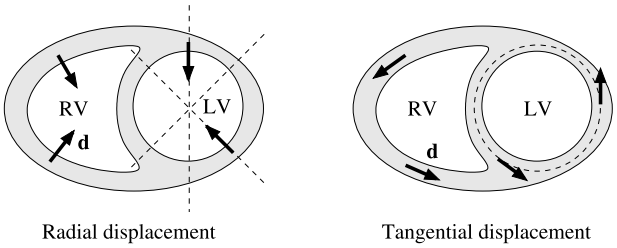

Figure 5. Relevant orientations for directional displacement measurement in short-axis views. For the LV, a polar coordinate system with origin at the LV gravity center is often used.

Assuming small deformations, a first-order Taylor expansion of Eq. 7 leads to:

$$\varepsilon_{\mathrm{v}} \approx Q_{\mathrm{v}} \tag{9}$$

so that, from Eq. 6, one has:

$$\varepsilon_{\mathrm{v}}^{(2)} \approx 2\varepsilon_{\mathrm{v}} \tag{10}$$

Defining strain from the strain tensor ($Q_{\mathbf{v}}$) or from variations of material segment length ($\varepsilon_{\mathbf{v}}$ and $\varepsilon_{\mathbf{v}}^{(2)}$) is therefore equivalent for small deformations. The latter assumption is always made in the literature.

Let us finally notice that the definitions of the (local) strain parameters $\varepsilon_{\mathbf{v}}$ and $\varepsilon_{\mathbf{v}}^{(2)}$ are similar to the shortening and ejection fraction (global) parameters. This relationship is investigated in Appendix C.

3.3.3.2. *Shear*. Off-diagonal elements E_{ij} ($i \neq j$) of the strain tensor define *shear strains* (Fig. 7). They relate to changes in angles between coordinate axes. More generally, distortion between two unit vectors **v** and **w** can be defined as:

$$Q_{\mathrm{vw}} := \mathrm{v}^T \mathrm{E} \mathrm{w} \tag{11}$$

For 3D displacement fields, three shear strains can be computed at each point, owing to the symmetry of **E**. Circumferential-radial, circumferential-longitudinal, and longitudinal-radial shears are measured by computing either the strain tensor in the RCL coordinate system (14, 15, 26), or the directional shears $Q_{\mathbf{vw}}$ along vectors **v** and **w** pointing in the circumferential and radial, circumferential and longitudinal, and longitudinal and radial directions, respectively.

As for strain, an alternate approach to shear considers angular variations between material segment pairs lying along given directions. Dealing with deformations between ED and ES then leads to defining the following shear measure, denoted by $\sigma_{\mathbf{vw}}$:

$$\sigma_{\mathrm{vw}} := \frac{\mathrm{dp}_{ES}^T \mathrm{dq}_{ES} - \mathrm{dp}_{ED}^T \mathrm{dq}_{ED}}{\|\mathrm{dp}_{ED}\| \, \|\mathrm{dq}_{ED}\|} \tag{12}$$

where ($\mathbf{dp}_{ED}$, $\mathbf{dq}_{ED}$) and ($\mathbf{dp}_{ES}$, $\mathbf{dq}_{ES}$) denote material segments pairs lying along unit vectors **v** (i.e., $\mathbf{dp} = \|\mathbf{dp}\|\mathbf{v}$) and **w** (i.e., $\mathbf{dq} = \|\mathbf{dq}\|\mathbf{w}$) at ED and ES, respectively. It is shown in Appendix B that:

$$\sigma_{\mathrm{vw}} := 2Q_{\mathrm{vw}} \tag{13}$$

From Eq. 11, shear is the (relative) variation of the scalar product $\mathbf{dp}_{ED}^T \mathbf{dq}_{ED}$. It is then possible to compute the *shear angle*, denoted by $\alpha_{\mathbf{vw}}$ and defined on Fig. 9. The computation, carried out in Appendix D, assumes that $\mathbf{dp}_{ED}$ and $\mathbf{dq}_{ED}$ are orthogonal. One obtains:

$$\sin \alpha_{\mathrm{vw}} = \frac{2Q_{\mathrm{vw}}}{(\varepsilon_{\mathrm{v}} + 1) + (\varepsilon_{\mathrm{w}} + 1)} \tag{14}$$

Where **v** and **w** are along the coordinate axes i and j, respectively, one has $Q_{\mathbf{vw}} = E_{ij}$, and, from Eq. 8, $\varepsilon_{\mathbf{v}} \approx E_{ii}$ and $\varepsilon_{\mathbf{w}} \approx E_{jj}$. Denoting then $\alpha_{\mathbf{vw}}$ as α_{ij}, one obtains the classical expression (35–37):

$$\sin \alpha_{ij} = \frac{2E_{ij}}{\sqrt{1 + 2E_{ii}}\sqrt{1 + 2E_{jj}}} \tag{15}$$

3.4.4. *Eigen-elements of the strain tensor*

The largest and smallest eigenvalues of the strain tensor **E** define the magnitude of maximal directional stretching and shortening, respectively. The companion eigenvectors are the mutually orthogonal unit vectors along which extremal deformations occur. Let **v** and **w** denote two distinct eigenvectors, and $E_{\mathbf{v}}$ and $E_{\mathbf{w}}$ the corresponding eigenvalues. One has:

$$Q_{\mathrm{v}}, = \mathrm{v}^T \mathrm{E} \mathrm{v} = E_{\mathrm{v}} \mathrm{v}^T \mathrm{v} = E_{\mathrm{v}} \tag{16}$$

$$Q_{\mathrm{vw}}, = \mathrm{v}^T \mathrm{E} \mathrm{w} = E_{\mathrm{w}} \mathrm{v}^T \mathrm{w} = 0 \tag{17}$$

Thus, the variation of the length of a material segment along an eigenvector is the associated eigenvalue. Moreover, two material segments lying along distinct eigenvectors remain perpendicular during deformation.

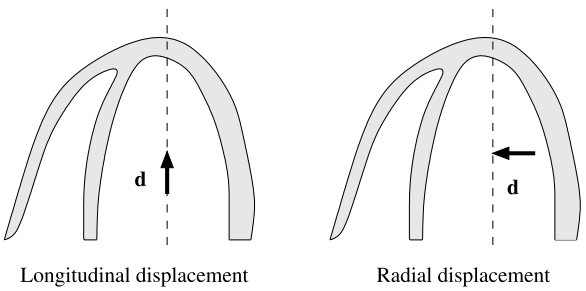

Figure 6. Relevant orientations for directional displacement measurement in long-axis views.

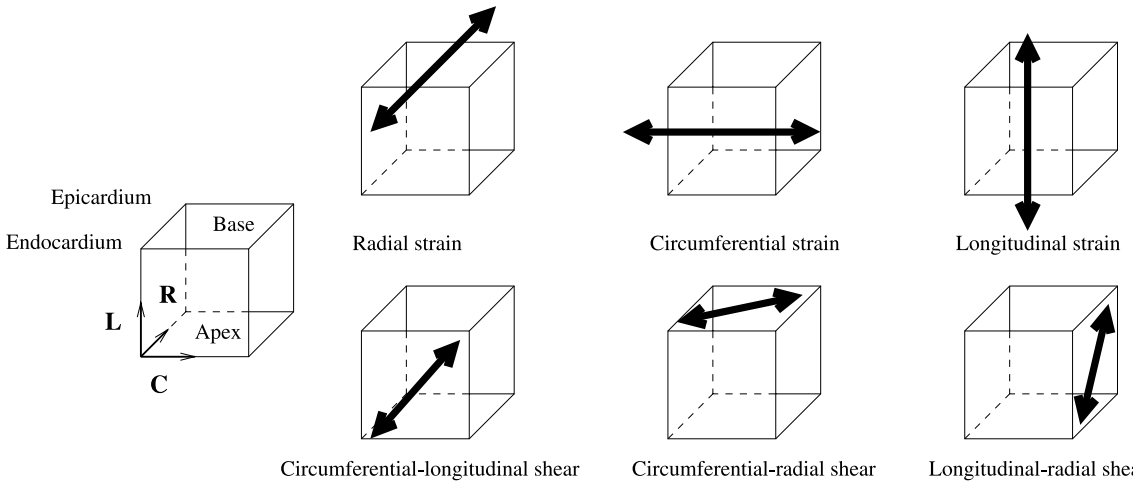

Figure 7. Strains and shears. Left is an undeformed volume element, that undergoes elementary deformations whose direction is indicated by the arrow.

3.5.5. *Dynamic analysis*

TS are based on sophisticated methods that assess frame-to-frame displacements and thus allow analyzing the evolution of deformation parameters during the cardiac cycle. In MS, motion is most often estimated between ED and ES, yielding static deformation parameters corresponding to systole. While all TS report dynamic temporal deformation data, only 3/20 MS do so (cf. Table 1).

3.3. *Myocardial segmentation*

3.1.1. *LV*

LV function varies regionally and usually differs longitudinally (i.e., at the base/apex), radially (i.e., at the endocardium/epicardium) and circumferentially (i.e., on septal/anterior/lateral/inferior[d] walls) (Fig. 10). Depending on the application and on the motion estimation method, deformation parameters can be visualized either as dense or segmental maps.

Dense mapping consists of displaying parameter values in pseudo colors at each point within the myocardium. Segmental mapping retains a single average value for each region of a myocardial segmentation, yielding a compact and concise description highlighting specific regional behavior. Two of 20 MS and 2/8 TS show dense parameter maps, which are clearly not a representation mode clinicians are familiar with today. Regarding segmental descriptions, the choice of a reference segmentation model is made difficult by the lack of anatomical landmarks in the myocardium. The American Heart Association (AHA) has made consensus recommendations that suggest a distribution of 35%, 35%, and 30% of the myocardial mass for the basal, mid, and apical levels, respectively (38). Slices should be circumferentially divided into six or four equal segments depending on the slice level, the septum being delineated by the attachment of the RV. This differentiation is not always taken into account as shown in Table 1.

[d]The inferior wall is also termed posterior (in particular, in echocardiography). The terminology inferior is, however, recommended [From Ref. (38)].

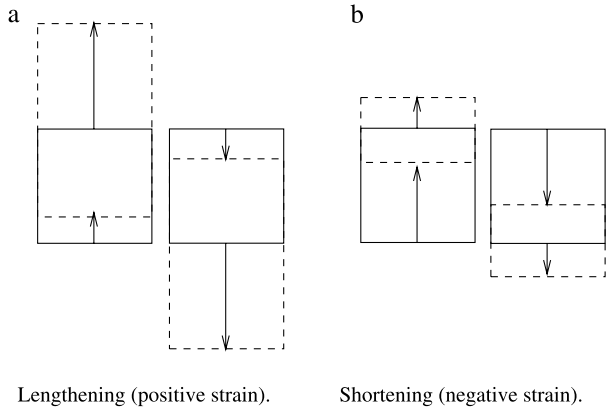

Figure 8. Normal strain depends both on the direction and spatial variations of displacement: displacements in a given direction can

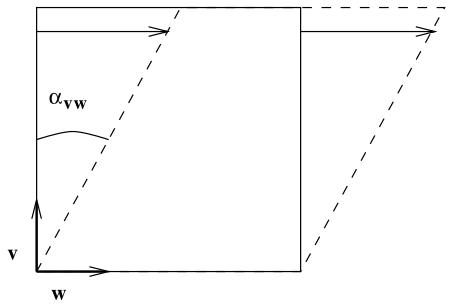

Figure 9. Shear angle between directions **v** and **w**.

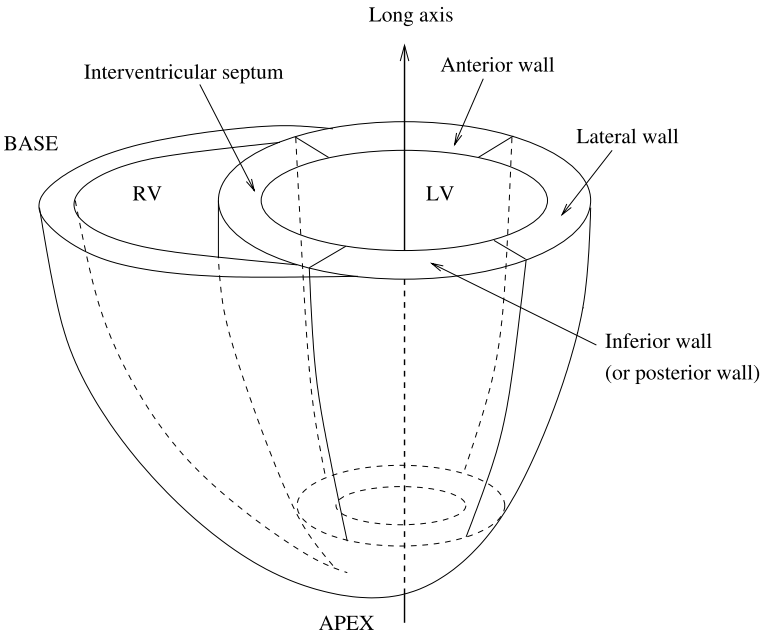

Figure 10. Myocardial walls.

3.2.2. *RV*

The inhomogeneity of the RV motion motivates a regional study of the RV kinematics. However, there is no standard convention for RV free wall (RVFW) segmentation. On long-axis images, the RVFW segmentation is similar to the LV segmentation and includes basal, mid, and apical levels. In short-axis views, the free wall is divided in three segments in Refs. (32, 34). In Fayad et al. (33), an anatomy-based segmentation is suggested, which divides the RVFW into four regions: RV outflow and inflow tracts, and mid-ventricular and apical regions.

3.4. *Statistical analysis*

Usual choices for comparing measurement distributions between myocardial regions or subject groups are Student's *t*-test, ANCOVA, ANOVA, and Mann-Whitney *U* test.

4. Quantification results and discussion

4.1. *LV radial contraction*

The values for radial displacement[e] for studies (26, 39) are listed in Table 3. All studies agree that myocardium is contracting radially towards the LV long axis. However, precisely describing this contraction can lead to contradictory conclusions. When analyzing regional function in the short-axis plane, radial contraction is maximal in the anterior/lateral walls (14, 23, 26) and in the inferior/lateral walls (39). Longitudinally, basal motion seems to be larger than apical motion (26), but it is not obvious in some studies (39, 40). The only study with a transmural differentiation for radial contraction concludes that endocardial contraction is larger than epicardial contraction (40).

The SD reported by Moore et al. (39) are high (SD_{mean} = 1.6 mm). This may originate from the fact that the resolution of the linear tag used in this study is poorer along the radial direction (only two to three tags over the myocardium) compared to the others. In Young et al. (26), SD is smaller (SD_{mean} = 0.9 mm). Here, a rectangular tag with isotropic and seemingly finer resolution is used.

It is difficult to draw conclusions for radial contraction under these conditions. Radial contraction is globally homogeneous and the associated displacement is 5 ± 1 mm over the whole myocardium.

Analyzing radial contraction dynamically reveals that it increases monotonically but heterogeneously depending on the segment and the slice level. A particular behavior for the interventricular septum has been noticed: the septum remains in a translated state during early diastole although inferior wall returns faster to its telediastolic position (14, 40). This specific motion could be caused by the RV (40).

4.2. *LV rotation*

All studies agree that myocardium undergoes a wringing motion induced by a basal clockwise rotation and an apical counterclockwise rotation, when seen from the apex (14, 18, 39–42). Table 4 clearly shows that the angle of

[e]In these studies, values have been reported as mean ± SD. For the sake of clarity, only mean values are provided in Table 3. High values for SD are mentioned in the text.

Table 3. Maximal radial displacements (mm) reported in studies (26) (n = 12) and (39) (n = 31)

		Septum	Anterior	Lateral	Inferior	Mean ± SD
Base	(26)	5.8	6.5	5.5	5.8	5.4 ± 1.0
	(39)	3.2	5.8	6.0	4.9	
Mid	(26)	6.1	6.3	5.8	5.7	5.1 ± 1.2
	(39)	3.0	3.7	5.2	5.2	
Apex	(26)	4.8	4.4	4.8	4.6	4.4 ± 1.0
	(39)	3.9	2.4	4.2	6.3	
Mean ± SD		4.5 ± 1.3	4.8 ± 1.6	5.2 ± 0.7	5.4 ± 0.6	

Positive values indicate inward (i.e., toward the centroid) motion.

rotation is larger at the apex ($10 \pm 2.3°$) than at the base ($4.4 \pm 0.4°$), and larger at the endocardium than at the epicardium (18, 31, 39, 40). Whereas maximal rotation angles are consistent at the basal level, a high variability is observed at the apex that may originate from disparities in apical level selection.

In the studies reporting a dynamic analysis, it has been noticed that the base rotates counterclockwise during early systole, reversing its motion later in systole (18, 26, 39). This time of reversing might be altered by certain pathologies. Maximal apical rotation occurs earlier than maximal basal rotation (43). Again, this may result from disparities in apical level selection.

4.3. *LV longitudinal contraction*

Longitudinal displacement is the most often computed zero-order parameter, certainly because of its relationship with the key problem of through-plane motion. Longitudinal contraction is directed towards the apex and decreases from base to apex (18, 26, 29, 39, 44).

The values for longitudinal displacement for studies (26, 29, 39, 44) are listed in Table 5. The homogeneity of measurements at a given level expresses the fact that the short-axis plane is almost uniformly translating perpendicular to the long-axis. At all levels, the inferior wall descends more than any other wall. Although the same qualitative conclusions can be drawn from all four studies (namely, largest displacement occurring at the base, in particular within the inferior segment), a discrepancy between the reported values is observed (up to 4.5 mm difference at the base).

The dynamic analysis of longitudinal contraction shows that displacement increases monotonically at basal and mid-ventricular levels, but not at the apex, where a transient motion towards the base has been noticed in the anterior wall (39).

4.4. *Radial strain*

Radial strain is positive in all regions during systole (23, 26), expressing therefore wall thickening. This is in accordance with an increase of radial displacement from the epicardium to the endocardium (Section 4.1). The values obtained in studies (23, 26, 36, 29) are listed[f] in Table 6. For Young et al. (26), radial strain is higher at the base and on the lateral wall. For Bogaert et al. (23) and Moore et al. (39), it is higher at the apex and on the anterior wall. This disparity echoes the inhomogeneity of radial displacement. One can also note the difference in the order of magnitude of the values reported in Young et al. (26) compared to other studies. Moreover, radial strain is higher at the endocardium than at the epicardium, which is the case of all first-order parameters (in a lesser extent, however, for longitudinal strain) (39).

As for radial contraction, SD is high in study (39) ($SD_{mean} = 22.7\%$) compared to (26) ($SD_{mean} = 8\%$) and (23) ($SD_{mean} = 1\%$). Notice that the latter study uses a sparse radial tagging pattern and computes radial strain from variations of wall thickness using the elongation formula.

4.5. *Circumferential strain*

Circumferential strain is the most frequently computed strain parameter. Table 7 shows that it is greater at the apex than at the base for all segments. This observation is corroborated by Ref. (23). Circumferential strain in anterior and lateral walls is higher than in inferior wall, as also noticed in Ref. (45). The largest inter-study dispersion occurs on the septum. Notice, however, that the SD of septal measurements reported in each study is not significantly higher than for the other segments.

In the early works (28, 46), the material segments used for computing circumferential elongation consist of pairs of tags oriented perpendicularly to the endocardium, which proves to be not equivalent to the above-mentioned strain definitions. This explains the difference with the other studies, as well as the higher SD due to the inhomogeneity of tag resolution.

[f]In studies (26, 39), measurements are provided for the four segments at the three levels. Since the data in study (23) are only available at each level and on each segment, as presented in Table 6, the values reported in Refs. (26, 39) have been averaged to allow for comparison at the same locations. The same approach has been used for longitudinal strain, shown in Table 9.

Table 4. Maximal rotation angles reported in studies (26) (n = 12), (18), (40) (n = 15), (42, 43) (n = 12)

	Base		Mid		Apex	
	Epicardial	Endocardial	Epicardial	Endocardial	Epicardial	Endocardial
(26)	− 4.2°		5.75°		13°	
(18)	− 4.8°	− 5°	–	–	8.5°	11°
(40)	− 4°	− 4°	5°	5°	9°	12°
(42, 43)	− 4.36°		–		6.8°	
Mean ± SD	− 4.4 ± 0.4°		− 5.2 ± 0.4°		10.0 ± 2.3°	

Positive values indicate counterclockwise rotation.

Table 5. Maximal longitudinal displacements (mm) reported in studies (26) (n = 12), (39) (n = 31), (29) (n = 6) and (44) (n = 19)

		Septum	Anterior	Lateral	Inferior	Mean ± SD
Base	(26)	11.9	11.3	12.8	14.2	11.2 ± 2.2
	(39)	8.1	7.1	8.8	10.6	
	(29)	10.8	10.2	9.2	12.3	
	(44)	10.0	12.8	13.3	15.2	
Mid	(26)	7.1	5.6	6.8	8.3	6.9 ± 1.0
	(39)	5.7	5.1	6.7	7.4	
	(29)	7.2	7.0	7.9	8.3	
	(44)	5.3	6.8	7.1	8.7	
Apex	(26)	1.6	0.8	2.0	2.7	2.6 ± 1.3
	(39)	3.5	2.3	4.9	4.8	
	(29)	2.4	2.4	3.6	3.8	
	(44)	1.0	1.7	0.8	3.0	
Mean ± SD		6.2 ± 3.6	6 ± 3.9	6.9 ± 3.8	8.3 ± 4.2	

Positive values indicate base-to-apex motion.

Table 6. Maximal radial strain (%) reported in studies (26) (n = 12), (39) (n = 31), (23) (n = 87) and (36) (n = 10)

	Septum	Anterior	Lateral	Inferior	Base	Mid	Apex
(26)	7	11	18.6	12	21	17.7	6.5
(39)	41	53.6	46.3	38.3	45	41.7	47.7
(23)	38.9	46.6	35.8	32.8	35	40.8	42
(36)	30	31	32	28	34	29	28
Mean ± SD	29.2 ± 15.6	35.5 ± 18.9	33.2 ± 11.4	27.7 ± 11.3	33.7 ± 9.8	32.3 ± 11.3	31 ± 18

Table 7. Maximal circumferential strain (%) reported in studies (46) (n = 10), (28) (n = 10), (26) (n = 12), (39) (n = 31) and (36) (n = 10)

		Septum	Anterior	Lateral	Inferior	Mean ± SD
Base	(46)	− 32	− 22	− 32	− 23	− 21.0 ± 4.2
	(28)	− 23	− 19	− 21	− 20	
	(26)	− 19	− 20	− 21	− 18	
	(39)	− 17	− 20	− 21	− 16	
	(36)	− 18.5	− 22	− 21	− 16	
Mid	(46)	− 34	− 25.5	− 27.5	− 31.5	− 22.5 ± 4.5
	(28)	− 23.5	− 23	− 21	− 21	
	(26)	− 20	− 22	− 21	− 19	
	(39)	− 16	− 23	− 22	− 16	
	(36)	− 20.5	− 23	− 24	− 18	
Apex	(46)	− 35	− 31	− 33	− 37	− 25.3 ± 5.1
	(28)	− 27	− 21	− 26	− 22	
	(26)	− 20	− 23	− 22	− 22	
	(39)	− 18	− 24	− 24	− 23	
	(36)	− 24	− 27	− 26	− 21	
Mean ± SD		− 23.1 ± 6.2	− 23.0 ± 3	− 24.1 ± 4	− 21.6 ± 5.8	

Table 8. Transmural variations of maximal circumferential strain (%) reported in studies (46) (n = 10), (28) (n = 10), (39) (n = 31) and (23) (n = 87)

	Epicardium	Mid-ventricle	Endocardium	Δ
(46)	− 22	− 30	− 44	22
(28)	− 17.2	− 22	− 27.2	10
(39)	− 14	− 20	− 26	12
(23)	− 15	n/a	− 38	23
Mean ± SD	− 17 ± 3.6	− 24 ± 5.3	− 33.8 ± 8.7	

Δ is the absolute difference between epicardium and endocardium values.

Table 9. Maximal longitudinal strain (%) reported in studies (26) (n = 12), (39) (n = 31), (23) (n = 87), (28) (n = 10) and (36) (n = 10)

	Septum	Anterior	Lateral	Inferior	Base	Mid	Apex
(28)					− 14.5	− 14	− 15.5
(26)	− 16	− 16.6	− 17.6	− 17.6	− 16.7	− 15.5	− 18.7
(39)	− 15.6	− 16.3	− 16	− 16	− 15	− 14.75	− 19
(23)	− 17.2	− 14.6	− 17.6	− 19.6	− 17.7	− 16.4	− 18.4
(36)	− 15.5	− 16	− 17.5	17	− 17	− 16	− 18
Mean ± SD	− 16 ± 0.8	− 15.9 ± 0.9	− 17.2 ± 0.8	− 17.5 ± 1.5	− 16.2 ± 1.4	− 15.3 ± 1	− 17.9 ± 1.4

Table 10. Maximal fiber and cross-fiber strains (%) reported in studies (24) (n = 10) and (23) (n = 87)

	Fiber		Cross-fiber	
	Epicardial	Endocardial	Epicardial	Endocardial
(24)	− 14	− 16	− 8	− 26
(23)	− 18	− 23.8	− 11.6	− 37.3

Table 11. Maximal shear strains (%) reported in studies (26) (n = 12) and (23) (n = 87)

	Septum			Anterior			Lateral			Inferior			Base			Mid			Apex		
	E_{cl}	E_{cr}	E_{lr}	E_{cl}	E_{cr}	E_{lr}	E_{cl}	E_{cr}	E_{lr}	E_{cl}	E_{cr}	E_{lr}	E_{cl}	E_{cr}	E_{lr}	E_{cl}	E_{cr}	E_{lr}	E_{cl}	E_{cr}	E_{lr}
(26)	3.3	2	0.3	3	1.3	−1	2.6	2.3	1.6	3.3	0.6	0	3.2	−4	1.7	3.5	2.5	0.9	2.5	1.7	1.5
(23)	11.3	−2.9	12.6	10.7	−4	3.1	8.4	0.4	9.3	8.2	0.4	17.2	10.6	10.7	8.1	9.6	−3.8	12.2	9	−13.9	11.7

Table 12. Largest eigenvalue E_1 reported in studies (26) (n = 12) and (39) (n = 31)

		Septum	Anterior	Lateral	Inferior	Mean ± SD
Base	(26)	23	20	26	22	34.5 ± 13
	(39)	46	43	53	43	
Mid	(26)	18	22	22	15	31.6 ± 14.3
	(39)	45	54	40	37	
Apex	(26)	10	8	12	5	30 ± 24.2
	(39)	42	69	51	43	
Mean ± SD		30.6 ± 15.6	36 ± 23.2	34 ± 16.6	27.5 ± 15.9	

Table 13. Smallest eigenvalue E_3 reported in studies (26) (n = 12) and (39) (n = 31)

		Septum	Anterior	Lateral	Inferior	Mean ± SD
Base	(26)	− 22	− 23	− 25	− 25	− 22.8 ± 1.6
	(39)	− 20	− 23	− 23	− 22	
Mid	(26)	− 23	− 25	− 24	− 23	− 23.5 ± 1.6
	(39)	− 21	− 26	− 24	− 22	
Apex	(26)	− 25	− 26	− 25	− 27	− 26 ± 1.3
	(39)	− 24	− 28	− 27	− 26	
Mean ± SD		− 22.5 ± 1.9	− 25.1 ± 1.9	− 24.9 ± 1.4	− 24.2 ± 2.1	

At last, circumferential shortening at the endocardium is greater than at the epicardium (23, 28, 39, 46), as shown in Table 8.

4.6. *Longitudinal strain*

Longitudinal strain, shown in Table 9, is negative during systole, therefore indicating shortening.

Contrary to longitudinal displacement, longitudinal shortening increases from base to apex. As underlined in Ref. (47), this indicates that the base undergoes mostly translation and is pulled down by the mid and apical sections of the ventricle. Whereas longitudinal displacement exhibits a strong variability between base and apex, longitudinal strain appears to be much more homogeneous.

4.7. *Fiber and cross-fiber strains*

Involving more anatomical knowledge and the use of autopsy results, fiber and cross-fiber strains have been computed in only two MS (Table 10). Fiber and cross-fiber directions show shortening, thus producing extensive thickening in the orthogonal direction (i.e., the radial direction), assuming isovolumic contraction. Because fibers in the midwall are circumferentially oriented, there may be a correlation between fiber shortening values [15% (24) or 21% (23)] and circumferential strain values (23% in average). Contrary to fiber shortening, which exhibits minor transmural variations, cross-fiber strain shows large variations (3.2 times higher for both studies) from the epicardium to the endocardium.

4.8. *Shear strains*

Shear strains are reported in only two studies (23, 26). Circumferential-longitudinal shear, denoted by E_{cl}, is induced by the LV torsion and the increase of longitudinal displacement from apex to base. As shown in Table 11, it is positive in all regions during systole, the order of magnitude varying considerably according to studies. Circumferential-radial shear, denoted by E_{cr}, is generated by the increase of rotation magnitude and the radial contraction about the central axis from epicardial to endocardial layers. As expected, it has opposite signs at the apex and the base. However, the studies do not agree on the sign. Longitudinal-radial shear, denoted by E_{lr}, shows no correlation between the two studies. Differences are likely to originate from the shear computation methods, based on the strain tensor in Ref. (26) and on a formula similar to elongation in Ref. (23).

4.9. *Eigenvalues and eigenvectors of the strain tensor*

The largest eigenvalue E_1 and smallest eigenvalue E_3 of the strain tensor **E** for studies (26, 39) are listed in Table 12 and Table 13, respectively. They correspond to normal strains along the principal stretching and shortening directions, respectively.

For both studies, E_1 varies similarly to E_{rr}. The associated eigenvector is radial, underlining the fact that the largest thickening occurs in the radial direction. The values for E_1 reported in Ref. (39) exhibit a large variability [SD_{mean} = 23% in Ref. (39) vs. SD_{mean} = 7.7% in Ref. (26)], echoing similar behaviors for the radial displacement and radial strain noticed in previous sections.

The values for E_3 are much more homogenous. The associated principal direction lies in the circumferential-longitudinal plane and is aligned with the direction of subepicardial fibers (26, 39) (Table 14). The largest shortening mainly occurs on the anterior wall and increases from base to apex.

4.10. *RV contraction*

Few studies have dealt with the RVFW behavior. Contraction in the RVFW is predominantly longitudinal (32, 34, 47, 48) and, to a lesser extent, radial. RVFW motion originates not only from LV motion but also from the RV itself. As noticed

Table 14. Angle of the eigenvector associated to eigenvalue E_3 with respect to circumferential direction, reported in Refs. (26) (n = 12) and (39) (n = 31)

	Mean ± SD	Max.	Min.
(26)	− 27.0 ± 8.1°	− 17°	− 47°
(39)	− 28.5 ± 10.7°	− 20°	− 30°

Table 15. RVFW shortening in the short-axis section reported in studies (34) (n = 16) and (33) (n = 10)

Reference	Base	Mid	Apex
(34)	− 14.3	− 12.8	− 16.5
(33)	− 17.3	− 19	− 22.4

Table 16. RVFW shortening in the longitudinal section reported in studies (32) (n = 9) and (33) (n = 10)

Reference	Base	Mid	Apex
(32)	− 34.7	− 22.6	− 31.3
(33)	− 27.6	− 20.5	− 24.7

in Ref. (47), it is difficult to identify a single axis about which to calculate contraction and rotation. Consequently, quantification is performed on a particular section and not along a particular direction. Strain, computed via the elongation formula, is the only deformation parameter that has been studied in the literature.

Shortening in the short-axis and longitudinal sections is shown in Table 15 and Table 16, respectively. As expected, longitudinal shortening is greater than short-axis shortening. For both parameters, shortening is in general greater at the apex and at the base than at the mid level.

5. Conclusions

MS and TS provide complementary approaches to measure myocardial strain using tagged MRI. The results reported for the normal human heart show common trends but also disparities.

5.1. *Results for the normal human heart*

Radial contraction is rather homogeneous over the LV and produces an inward displacement of 5 ± 1 mm. It is the greatest thickening experienced by the tissue. LV twisting is induced by a − 4.4 ± 0.4° clockwise rotation at the base and a 10 ± 2.3° counterclockwise rotation at the apex. An initial counterclockwise rotation of the base has been noticed in early systole. Circumferential strain has an average value of − 23 ± 4.9% and is greater at the endocardium than at the epicardium, at the apex than at the base, and on anterior and lateral walls. Longitudinal contraction involves 1) a displacement that increases from base (11.2 ± 2.2 mm) through mid level (6.9 ± 1.0 mm) to apex (2.6 ± 1.3 mm), and is slightly larger in the inferior wall; and 2) a quite uniform strain, indicating that the base is pulled down by the apical region. Subepicardial fiber direction (−27.7 ± 1°) is the greatest shortening direction.

Regarding the RV, shortening is larger in the long-axis (26.9 ± 5.4%) than in the short-axis (17 ± 3.4%) incidence. For the two incidences, shortening magnitudes are generally higher at the apex and at the base.

5.2. *Disparities in quantification results*

Disparities for qualitative observations concern the myocardium behavior along the radial direction: results diverge regarding the location of the greatest radial displacement (apex vs. base, inferior vs. anterior wall).

Regarding quantitative results, disparities can have multiple origins: population inhomogeneity, variations of the locations of slice level, use of different motion estimation and quantification methods, etc. Determining the influence of these factors on measurements requires consideration of deformation parameters globally rather than individually. The two most complete studies [i.e., Refs. (26) and (39)] highlight different results for radial displacement, longitudinal contraction, and radial strain, whereas converging for circumferential and longitudinal strains. Regarding radial parameters, low tag resolution, which has been noticed to induce high measurement variability for study (39), could also be the cause of inter-study disparities. Moreover, Table 5 suggests that slice levels are more distant in Ref. (26) than in Ref. (39). This may explain the differences for longitudinal contraction. If this hypothesis is confirmed, it is not surprising that circumferential and longitudinal strains are not affected, given that first-order parameters are insensitive to global translational motion.

5.3. *Perspectives*

In the future, complying with the recently issued AHA recommendations (38), in particular for selecting slice levels, could provide an objective basis for comparing myocardial strain measurements from tagged MRI as well as from different imaging modalities. In addition, some information, such as population characteristics and tag spacing, should be mandatorily reported.

The present review could serve as a comparison tool for future studies, would they deal with the healthy heart or with specific pathologies. The perspectives of this work concerns 1) incorporating quantification results from phase contrast MRI and other imaging strain modalities (strain-rate imaging), and 2) constructing and validating quantitative functional models for the healthy heart as well as for designated classes of pathologies.

Appendix

A. *Relating strain definitions*

Consider a small material segment with end points ($\mathbf{x}_1$, $\mathbf{x}_2$) at ED, and ($\mathbf{x}'_1$, $\mathbf{x}'_2$) at ES. From Eq. 1, one has:

$$\begin{aligned} \mathrm{dp}_{ES} &= \mathrm{x}'_2 - \mathrm{x}'_1 \\ &= \mathrm{f}(\mathrm{x}_2) - \mathrm{f}(\mathrm{x}_1) \\ &\approx \nabla \mathrm{f}\ [\mathrm{x}_2 - \mathrm{x}_1] = \mathrm{F}\ \mathrm{dp}_{ED} \end{aligned}$$

The segment length at ES is then:

$$\begin{aligned} \|\mathrm{dp}_{ES}\|^2 &= \mathrm{dp}_{ES}^T \mathrm{dp}_{ES} \\ &= \mathrm{dp}_{ED}^T \mathrm{F}^T \mathrm{F}\ \mathrm{dp}_{ED} \end{aligned}$$

Since $\mathbf{dp}_{ED} = \|\mathbf{dp}_{ED}\|\mathbf{v}$, it follows:

$$\begin{aligned}\|\mathrm{dp}_{ES}\|^2 - \|\mathrm{dp}_{ED}\|^2 &= \mathrm{dp}_{ED}^T(\mathrm{F}^T\mathrm{F} - \mathrm{Id})\mathrm{dp}_{ED} \\ &= 2\|\mathrm{dp}_{ED}\|^2\mathrm{v}^T\mathrm{E}\mathrm{v} \\ &= 2\|\mathrm{dp}_{ED}\|^2 Q_{\mathrm{v}}\end{aligned}$$

Using definition (5), we conclude:

$$\varepsilon_{\mathrm{v}}^{(2)} = \frac{\|\mathrm{dp}_{ES}\|^2 - \|\mathrm{dp}_{ED}\|^2}{\|\mathrm{dp}_{ED}\|^2} = 2Q_{\mathrm{v}}$$

B. *Relating shear definitions*

Similarly, one has:

$$\begin{aligned}\mathrm{dp}_{ES} &= \mathrm{F}\ \mathrm{dp}_{ED} \\ \mathrm{dq}_{ES} &= \mathrm{F}\ \mathrm{dq}_{ED}\end{aligned}$$

Computing the scalar product between $\mathbf{dp}_{ES}$ and $\mathbf{dq}_{ES}$ yields:

$$\begin{aligned}\mathrm{dp}_{ES}^T\mathrm{dq}_{ES} &= (\mathrm{F}\ \mathrm{dp}_{ED})^T\mathrm{F}\ \mathrm{dq}_{ED} \\ &= \mathrm{dp}_{ED}^T\mathrm{F}^T\mathrm{F}\ \mathrm{dq}_{ED} \\ &= \mathrm{dp}_{ED}^T(2\mathrm{E} + \mathrm{Id})\mathrm{dq}_{ED} \\ &= 2\mathrm{dp}_{ED}^T\mathrm{E}\ \mathrm{dq}_{ED} + \mathrm{dp}_{ED}^T\mathrm{dq}_{ED}\end{aligned}$$

Since $\mathbf{dp}_{ED} = \|\mathbf{dp}_{ED}\|\mathbf{v}$ and $\mathbf{dq}_{ED} = \|\mathbf{dq}_{ED}\|\mathbf{w}$, it follows:

$$\begin{aligned}\mathrm{dp}_{ES}^T\mathrm{dq}_{ES} - \mathrm{dp}_{ED}^T\mathrm{dq}_{ED} &= 2\mathrm{dp}_{ED}^T\mathrm{E}\ \mathrm{dq}_{ED} \\ &= 2\|\mathrm{dp}_{ED}\|\ \|\mathrm{dq}_{ED}\|\mathrm{v}^T\mathrm{E}\mathrm{w} \\ &= 2\|\mathrm{dp}_{ED}\|\ \|\mathrm{dq}_{ED}\|Q_{\mathrm{vw}}\end{aligned}$$

We conclude:

$$\sigma_{\mathrm{vw}} = \frac{\mathrm{dp}_{ES}^T\mathrm{dq}_{ES} - \mathrm{dp}_{ED}^T\mathrm{dq}_{ED}}{\|\mathrm{dp}_{ED}\|\ \|\mathrm{dq}_{ED}\|} = 2Q_{\mathrm{vw}}$$

C. *Ejection and shortening fractions*

The *shortening fraction* (*SF*) is defined as:

$$SF := \frac{D_{ED} - D_{ES}}{D_{ED}}$$

where D_{ED} and D_{ES} denote the diameter of the LV cavity at ED and ES, respectively. This expression appears to be similar to the definition (9) for elongation $\varepsilon_{\mathbf{v}}$, assuming $\mathbf{v}$ originates radially from the LV cavity center.

The ejection fraction (*EF*) is defined as:

$$EF := \frac{V_{ED} - V_{ES}}{V_{ED}}$$

where V_{ED} and V_{ES} stand for the volume of the LV cavity at end ED and ES, respectively. Using the Teicholz formula (49) for approximating volumes by the square of diameters yields:

$$EF \approx \frac{D_{ED}^2 - D_{ES}^2}{D_{ED}^2}$$

revealing a similarly with the strain measure $\varepsilon_{\mathbf{v}}^{(2)}$ for $\mathbf{v}$ defined as before.

Assuming small deformations, the relationship (9) therefore implies:

$$EF \approx 2SF$$

This approximately holds for normal subjects for which $SF = 30 \pm 5\%$ and $EF = 67 \pm 10\%$ (50, 51).

D. *Shear angle*

For orthogonal material segments $\mathbf{dp}_{ED}$ and $\mathbf{dq}_{ED}$, Eq. 13 reduces to:

$$\frac{\mathrm{dp}_{ES}^T\mathrm{dq}_{ES}}{\|\mathrm{dp}_{ED}\|\ \|\mathrm{dq}_{ED}\|} = 2Q_{\mathrm{vw}}$$

Since $\mathbf{dp}_{ES}^T\mathbf{dq}_{ES} = \|\mathbf{dp}_{ES}\|\ \|\mathbf{dq}_{ES}\|\cos(\pi - \alpha_{\mathbf{vw}})$, it follows:

$$\cos(\pi - \alpha_{\mathrm{vw}}) = 2Q_{\mathrm{vw}}\frac{\|\mathrm{dp}_{ES}\|\ \|\mathrm{dq}_{ES}\|}{\|\mathrm{dp}_{ED}\|\ \|\mathrm{dq}_{ED}\|}$$

Using Eq. 4, one obtains finally:

$$\sin\alpha_{\mathrm{vw}} = \frac{2Q_{\mathrm{vw}}}{(\varepsilon_{\mathrm{v}} + 1)(\varepsilon_{\mathrm{w}} + 1)}$$

References

1. Zerhouni E, Parish D, Rogers W, Yang A, Shapiro E. Human heart: tagging with MR imaging—a method for non invasive assessment of myocardial motion. Radiology 1988; 169(1):59–63.
2. Axel L, Dougherty L. MR imaging of motion with spatial modulation of magnetization. Radiology 1989; 171(3):841–845.
3. Rademakers F, Buchalter M, Rogers W, Zerhouni E, Weisfeldt M, Weiss J, Shapiro E. Dissociation between left ventricular untwisting and filling—accentuation by catecholamines. Circulation 1992; 85:1572–1581.
4. Azhari H, Weiss J, Rogers W, Siu C, Zerhouni E, Shapiro E. Non-invasive quantification of principal strains in normal canine hearts using tagged MRI images in 3-D. Am J Physiol 1993; 264:205–216.
5. Bogaert J, Bosmans H, Maes A, Suetens P, Marchal G, Rademakers F. Remote myocardial dysfunction after acute myocardial in 39 farction: impact of left ventricular shape on regional function. J Am Coll Radiol 2000; 35(6):1525–1534.
6. Götte M, van Rossum A, Twisk J, Kuijer J, Marcus J, Visser C.

Quantification of regional contractile function after infarction: strain analysis superior to wall thickening in discriminating infarct from remote myocardium. J Am Coll Radiol 2001; 37(3):808–817.
7. Ennis D, Epstein F, McVeigh E, Arai A. MR tagging of the entire cardiac cycle: regional analysis of normal subjects an hypertrophic cardiomyopathy using a new quantity for assessment of regional cardiac function. In: Meeting of the International Society for Magnetic Resonance in Medicine (ISMRM'01). Glasgow, UK, 2001.
8. Mosher T, Smith M. A DANTE tagging sequence for the evaluation of translational sample motion. Magn Reson Med 1990; 15:334–339.
9. Fischer S, McKinnon G, Maier S, Boesiger P. Improved myocardial tagging contrast. Magn Reson Med 1993; 30:191–200.
10. Amini A, Prince J. Measurement of Cardiac Deformations from MRI: Physical and Mathematical Models, Vol. 23 of Computational Imaging and Vision. Dordrecht, The Netherlands: Kluwer Academic Publishers, 2001.
11. Osman N, Prince J. Imaging heart motion using harmonic phase MRI. IEEE Trans Med Imag 2000; 19(3):186–202.
12. Kraitchman D, Young A, Chang C, Axel L. Semi-automatic tracking of myocardial motion in MR tagged images. IEEE Trans Med Imag 1995; 14(3):422–433.
13. Guttman M, Prince J, McVeigh E. Tag and contour detection in tagged MR images of the left ventricle. IEEE Trans Med Imag 1994; 13(1):74–88.
14. Declerck J, Ayache N, McVeigh E. Use of a 4D Planispheric Transformation for the Tracking and the Analysis of LV Motion with Tagged MR Images. Technical Report 3535. Sophia-Antipolis: INRIA, 1998.
15. Clarysse P, Basset C, Khouas L, Croisille P, Friboulet D, Odet C, Magnin I. Two-dimensional spatial and temporal displacement and deformation field fitting from cardiac magnetic resonance imaging. Med Image Anal 2000; 4(4):253–268.
16. Axel L, Gonçalves R, Bloomgarden D. Regional heart wall motion: two-dimensional analysis and functional imaging of regional heart wall motion with magnetic resonance imaging. Radiology 1992; 183:745–750.
17. Oldershaw P, Bishop A. The difficulty of assessing right ventricular function. Br Heart J 1995; 74:99–100.
18. Park J, Metaxas D, Young A, Axel L. Analysis of left ventricular wall motion based on volumetric deformables models and MRI-SPAMM. Med Image Anal 1996; 1(1):53–71.
19. Hsu E, Muzikant A, Matulevicius S, Penland R, Henriquez C. Magnetic resonance myocardial fiber orientation mapping with direct histological correlation. Am J Physiol 1998; 274:1627–1634.
20. Scollan D, Holmes A, Winslow R, Forder J. Histological validation of myocardial microstructure obtained from diffusion tensor magnetic resonance imaging. Am J Physiol 1998; 275:2308–2318.
21. O'Dell W, Wedeen V, Reese T, McCulloch A. Histological validation of MR diffusion imaging for myocardial fiber architecture analysis. In: Meeting of the International Society for Magnetic Resonance in Medicine (ISMRM'97). Vancouver, Canada, 1997.
22. Dou J, Tseng W, Reese T, Wedeen V. Combined diffusion and strain MRI reveals structure and function of human myocardial laminar sheets in vivo. Magn Reson Med 2003; 50(1):107–113.
23. Bogaert J, Rademakers F. Regional nonuniformity of normal adult human left ventricle. Am J Physiol, Heart Circ Physiol 2001; 280:610–620.
24. MacGowan G, Shapiro E, Azhari H, Siu C, Hees P, Hutchins G, Weiss J, Rademakers F. Noninvasive measurement of shortening in the fiber and cross-fiber directions in the normal human left ventricle and in idiopathic dilated cardiomyopathy. Circulation 1997; 96:535–541.
25. Young A, Imai H, Chang C, Axel L. Two-dimensional left ventricular deformation during systole using magnetic resonance imaging with spatial modulation of magnetization. Circulation 1994; 89(2):740–752.
26. Young A, Kramer C, Ferrari V, Axel L, Reichek N. Three-dimensional left ventricular deformation in hypertrophic cardiomyopathy. Circulation 1994; 90:854–867.
27. Wang Y-P, Chen Y, Amini A. Efficient LV motion estimation using subspace approximation techniques. IEEE Trans Med Imag 2001; 20(6):499–513.
28. Kramer C, Reichek N, Ferrari V, Theobald T, Dawson J, Axel L. Regional heterogeneity of function in hypertrophic cardiomyopathy. Circulation 1994; 90:186–194.
29. Dong S-J, MacGregor J, Crawley A, McVeigh E, Belenkie I, Smith E, Tyberg J, Beyar R. Left ventricular wall thickness and regional systolic function in patients with hypertrophic cardiomyopathy—a three-dimensional tagged magnetic resonance imaging study. Circulation 1994; 90:1200–1209.
30. Chai J-W, Chen Y -T, Lee S-K. MRI assessment of regional heart wall motion in the longitudinal axis sections of left ventricle by spatial modulation of magnetization. Chin Med J 1997; 60(1):13–20.
31. Garot J, Bluemke D, Osman N, Rochitte C, McVeigh E, Zerhouni E, Prince J, Lima J. Fast determination of regional myocardial strain fields from tagged cardiac images using harmonic phase MRI. Circulation 2000; 101(9):981–988.
32. Naito H, Arisawa J, Harada K, Yamagami H, Kozuka T, Tamura S. Assessment of right ventricular regional contraction and comparison with the left ventricle in normal humans: a cine magnetic resonance study with presaturation myocardial tagging. Br Heart J 1995; 74:186–191.
33. Fayad Z, Ferrari V, Kraitchman D, Young A, Palevsky H, Bloomgarden D, Axel L. Right ventricular regional function using MR tagging: normals versus chronic pulmonary hypertension. Magn Reson Med 1998; 39:116–123.
34. Klein S, Graham T, Lorenz C. Noninvasive delineation of normal right ventricle contractile motion with magnetic resonance imaging myocardial tagging. Ann Biomed Eng 1998; 26:756–763.
35. Fung Y. A First Course in Continuum Mechanics. 3rd Ed. Upper Saddle River, NJ: Prentice Hall, 1993.
36. Kuijer J, Marcus J, Gtte M, van Rossum A, Heethaar R. Threedimensional myocardial strains at end-systole and during diastole in the left ventricle of normal humans. J Cardiovasc Magn Reson 2002; 4(3):341–351.
37. Oxenham H, Young A, Cowan B, Gentles T, Occleshaw C, Fonseca C, Doughty R, Sharpe N. Age-related changes in myocardial relaxation using three-dimensional tagged magnetic resonance imaging. J Cardiovasc Magn Reson 2003; 5(3):421–430.
38. Cerqueira M, Weissman N, Dilsizian C, Jacobs A, Kaul S, Laskey W, Pennell D, Rumerger J, Ryan T, Verani M. Standardized myocardial segmentation and nomenclature for tomographic imaging of the heart. Circulation 2002; 105:539–542.
39. Moore C, Lugo-Olivieri C, McVeigh E, Zerhouni E. Three dimensional systolic strain patterns in the normal human left ventricle: characterization with tagged MR imaging. Radiology 2000; 214(2):453–466.
40. Allouche C, Makram-Ebeid S, Ayache N, Delingette H. A new kinetic modeling scheme for the human left ventricle wall motion analysis with MR-tagging imaging. In: Katila T, Magnin I, Clarysse P, Montagnat J, Nenonen J, eds. Functional Imaging and Modeling of the Heart (FIMH'01), Vol. 2230 of Lecture Notes in Computer Science, Helsinki, Finland, 2001:61–68.
41. Allouche C, Makram-Ebeid S, Stuber M, Ayache N, Delingette H. New methods and algorithms for the accurate, real-time, motion analysis of the left ventricule with MRI-tagging. In: Computer Assisted Radiology and Surgery (CARS'2001). Vol. 1230. Berlin, Germany, 2001:911–916.
42. Stuber M, Scheidegger M, Fischer S, Nagel E, Steinemann F. Alterations in the local myocardial motion pattern in patients suffering from pressure overload due to aortic stenosis. Circulation 1999; 100:361–368.
43. Nagel E, Stuber M, Burkhard B, Fischer S, Scheidegger M, Boesiger

P, Hess O. Cardiac rotation and relaxation in patients with aortic valve stenosis. Eur Heart J 2000; 21:582–589.
44. Rogers W, Shapiro E, Weiss J, Buchalter M, Rademakers F, Weisfeldt M, Zerhouni E. Quantification of and correction for left ventricular systolic long axis shortening by magnetic resonance tissue tagging and slice isolation. Circulation 1991; 84:721–731.
45. Dornier C, Ivancevic M, Lecoq G, Righetti A, Vallée J. Automatic classification of myocardial segments by tagMRI and by use of a healthy myocardial atlas. In: European Society for Magnetic Resonance in Medicine and Biology. Cannes, France, 2002:105.
46. Clark N, Reichek N, Bergey P, Hoffman E, Brownson D, Palmon L, Axel L. Circumferential myocardial shortening in the normal human left ventricle: assessment by magnetic resonance imaging using spatial modulation of magnetization. Circulation 1991; 84:67–74.
47. Haber I, Metaxas D, Axel L. Three-dimensional motion reconstruction and analysis of the right ventricle using tagged MRI. Med Image Anal 1998; 4(4):335–355.
48. Young A, Fayad Z, Axel L. Right ventricular midwall surface motion and deformation using magnetic resonance tagging. Am J Physiol, Heart Circ Physiol 1996; 271:2677–2688.
49. Teicholz L, Kreulen T, Herman M, Gorlin R. Problems in echocardiographic volume determinations: echocardiographic-angiographic correlations in the presence or absence of asynergy. Am J Cardiol 1976; 37:7–11.
50. Sutton P. Measurements in Cardiology. Boca Raton, FL: CRC Press, 1999.
51. Pennell D. Ventricular volume and mass by CMR. J Cardiovasc Magn Reson 2002; 4(3):507–513.